A&A 515, A69 (2010)
DOI: 10.1051/0004-6361/200913142

Astronomy & Astrophysics

First step to detect an extrasolar planet using simultaneous observations with the VLTI instruments AMBER and MIDI⋆

A. Matter[1], M. Vannier[2], S. Morel[3], B. Lopez[1], W. Jaffe[4], S. Lagarde[1], R. G. Petrov[2], and C. Leinert[5]

[1] Laboratoire Fizeau, UMR 6525, UNS - Observatoire de la Côte d'Azur, BP 4229, 06304 Nice Cedex 4, France
e-mail: matter@oca.eu
[2] Laboratoire Fizeau, UMR 6525, UNS - Observatoire de la Côte d'Azur, 06108 Nice Cedex 02, France
[3] ESO, Casilla 19001, Vitacura, Santiago 19, Chile
[4] Leiden Observatory, PO Box 9513, 2300 RA, Leiden, The Netherlands
[5] MPIA, Königstuhl 17, 69117 Heidelberg, Germany

Received 19 August 2009 / Accepted 8 January 2010

ABSTRACT

Aims. Performed in November 2007 as a part of the MIDI Guaranteed Time Observation Exoplanet Programme, the observation of Gliese 86b constituted the first attempt at an exoplanet detection with the VLTI instrument MIDI. It is also a technical achievement since it motivated the first VLTI observation using AMBER and MIDI simultaneously.
Methods. Fringes were obtained for both instruments with the aim of reaching sufficient precision on the low differential phase signal of Gliese 86b. The principle is to correct the phase measured in N-band from the water vapour dispersion using the fringes in K-band. In N-band, the source, Gliese 86, has an estimated magnitude of 3.8. With a separation of 0.11 AU, a flux ratio of about 10^{-3} is expected between the planet and the star. According to the measurement principle and the planet signal signature, the effective expected interferometric phase is a curved-like function of the wavelength with a mean amplitude of about 0.03°.
Results. Based on the MIDI phase measurements of the calibrator HD 9362, our study shows that a precision on the curvature measurement of about 0.33° is currently reached. Consequently, we stand at a factor 10 above the phase signal from the planet. The AMBER data, obtained in parallel, were too noisy to extrapolate and to remove the corresponding dispersion in N band at the required level of precision. However, we report the set of data obtained, we discuss the calibration process involved, and we estimate its theoretical efficiency.

Key words. instrumentation: interferometers – techniques: interferometric – planetary systems – infrared: general – atmospheric effects

1. Introduction

The mid-infrared spectral domain is of interest for observing the surrounding hot dust around young stars or around the active galactic nuclei. It is as well adapted to the observing close-in extrasolar giant planets (EGP), which are signicantly luminous in this wavelength domain. Since the discovery in 1995 of a hot Jupiter-like planetary companion orbiting 51 Peg by Mayor & Queloz (1995), the indirect method of precision radial velocimetry has provided a large harvest of about 320 extrasolar planets detection, yielding orbital distance, eccentricity, and lower mass estimates. Among those few planets whose orbital plane is oriented edge-on to the Earth, the transit method has been able to provide unique constraints on the atmosphere composition of some planets like HD 209458b with the Spitzer Space Telescope (Richardson et al. 2007).

In this framework, differential interferometry represents an innovative direct detection method that may allow observers to obtain spectroscopic information, planetary mass, and orbit inclination of extrasolar planets around nearby stars using the current ground-based long-baseline interferometers, such as the VLTI (Segransan et al. 2000; Lopez et al. 2000) or the Keck Interferometer (Vasisht & Colavita 2004). Nowadays differential interferometry, our focus in this paper, should allow observations of close-in extrasolar giant planets (Joergens & Quirrenbach 2004; Vannier et al. 2006), while exo-earth characterization will require the use of nulling techniques on space experiments.

The VLTI (Very Large Telescope Interferometer) allows coherent combination, in the near and mid-infrared, of the light collected by the 8-m Unit Telescopes (UTs) or by the 1.8-m auxiliary telescopes (ATs). Currently, a three-beam near-IR instrument, AMBER (Petrov & Amber Consortium 2003), and a two-beam mid-IR instrument, MIDI (Leinert et al. 2003), are available.

Detection and characterization of close-in EGPs may be foreseen with the MIDI instrument by using differential phase. In fact, for our observed source, Gliese 86b, the flux ratio is much more favourable in N band ($\approx 10^{-3}$) than in the near infrared ($\approx 10^{-5}$) or the visible ($\approx 10^{-6}$) (see Fig. 1); however, instrumental and atmospheric stability introduce some limitations. In N band, two contributions can strongly affect the interferometric measurements: the overwhelming sky background emission, and the strong chromatic dispersion due to the water vapour (Meisner & Le Poole 2003; Colavita et al. 2004). While the former can be generally removed by subtracting the two interferometric channels of MIDI, the contribution of the latter appears very limiting and difficult to calibrate. Nevertheless the strong chromatic dependence of the flux ratio between the planet and the star, could help in that case.

⋆ Based on GTO observations collected at the European Southern Observatory, Chile (ESO number: 080.C-0344).

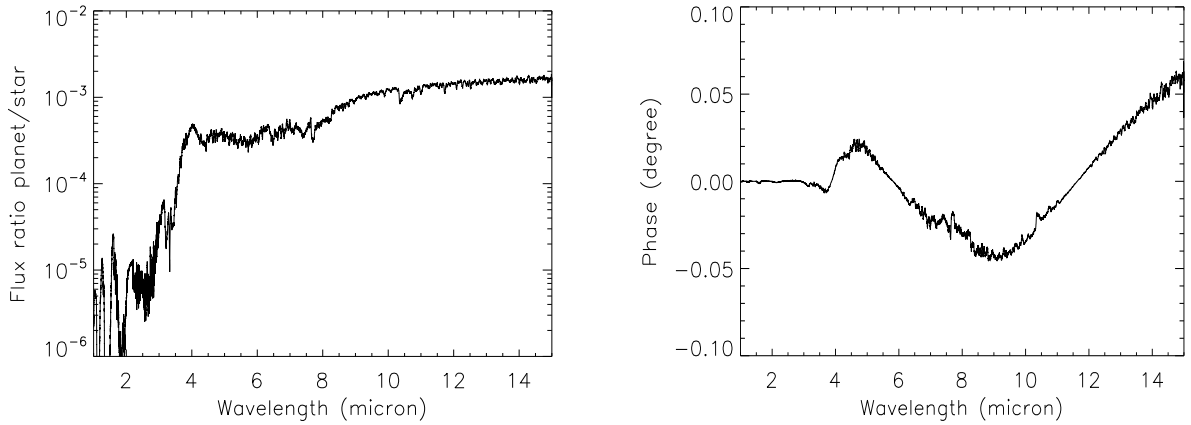

Fig. 1. *Left panel*: expected flux ratio between Gliese 86b and its star between 1 and 15 μm. *Right panel*: theoretical interferometric phase of the GL86 system between 1 and 15 μm; the projected baseline used here is equal to 110 m for a baseline value of 130 m at ground level. For these two figures, which have been smoothed for sake of clarity, the planetary radius is assumed to be 1.2 $R_{\rm jupiter}$ and the planetary flux model is the one provided by Barman that is described in Sect. 2.3.

As described later in that paper, the flux ratio, hence the interferometric phase signal of Gliese 86b, is negligible in the near infrared (1 to 2.5 μm) (see Fig. 1). Therefore to measure and correct the water vapour dispersion, one solution would be to use AMBER simultaneously as an estimator of the dispersion amplitude. Then, an extrapolation to the N-band could be applied to correct the MIDI data. This approach would allow a N-band chromatic water vapour modelling that would preserve the planetary signal.

In this article, we first present the physical features of the planetary system and the theoretical phase signature of the exoplanet Gliese 86b. In the second section, the atmospheric and instrumental perturbations are addressed, along with the principle of estimation and extrapolation of the dispersion amplitude from near to mid-infrared. The effective astrophysical signal from the planet is estimated in Sect. 3. The technical aspects and the sequence of the simultaneous observations are explained in Sect. 4. In the last section, the performance of the extrapolation method is evaluated from the AMBER data set obtained from these observations. In addition, we present an estimation of the accuracy achieved on MIDI phase measurements without the use of AMBER data.

2. Features of the system and theoretical signal

2.1. Features of the Gliese 86 system

Gliese 86 is a high proper motion star, located 10.9 pc from our Sun. It presents the features of a bright ($m_V = 6.12$ and $m_N = 3.8$) early K dwarf whose main physical parameters are $B - V = 0.81$, $T_{\rm eff} = 5350$ K, $\log(g) = 4.6$ (Flynn & Morell 1997). Its absolute magnitude is 6.2, yielding a luminosity $L = 0.27\ L_{\odot}$. This star bears all the characteristics of a few billion years-old K dwarf from the old disk population, including a slightly poor metal content ([Fe/H] = −0.24) (Flynn & Morell 1997).

In 2000, a planetary companion identified as Gliese 86b has been detected by radial velocimetry (Queloz et al. 2000). This companion is close to its parent star, with a 0.11 AU semi-major axis and an angular separation of about 10 mas. It has a minimum mass of about 4 $M_{\rm J}$, a rotating period of 15.76 days and a very low eccentricity of 0.04. This source bears all the characteristics of a typical close-in EGP.

2.2. Theoretical interferometric signal

The observation of a source with a two-telescope interferometer gives access to two observables: the modulus and the phase of the complex visibility, respectively, corresponding to the contrast (or visibility) and the position of the fringe pattern.

The Van Cittert & Zernike theorem allows linking these observables to the modulus and the phase of the Fourier transform of the brightness distribution of the source. In the case of a planetary system for which the star appears as a uniform disk of constant angular diameter D_*, and the planet appears as a point-like source, we consider the following brightness distribution:

$$I(\theta, \lambda) = I_{\rm star}(\lambda)\ \Pi\left(\frac{\theta}{D_*}\right) + I_{\rm planet}(\lambda)\ \delta(\theta - \rho). \quad (1)$$

We indicate by $I_{\rm star}(\lambda)$ and $I_{\rm planet}(\lambda)$ the monochromatic flux of the two components, separated by an angular distance ρ. The Π symbol represents the uniform disk function equal to 1 inside and 0 outside, and describing the brightness distribution of the star. The symbol θ is the angular coordinate in the plane of the sky, with the origin taken on the stellar component.

The plane of spatial frequency, defined by the vector $\boldsymbol{w}(u, v)$, is covered by a single-baseline interferometer and the u-axis vector is chosen along the interferometric baseline vector $\boldsymbol{B}$ (with $\boldsymbol{u} = \frac{\boldsymbol{B}}{\lambda}$). The Fourier transform $\hat{I}(\boldsymbol{w}, \lambda)$ of the brightness distribution in this plane is

$$\hat{I}(\boldsymbol{w}, \lambda) = \mathrm{C}_*(u) I_{\rm star}(\lambda) + I_{\rm planet}(\lambda) \mathrm{e}^{-\mathrm{i}2\pi \boldsymbol{u}\cdot\boldsymbol{\rho}}, \quad (2)$$

where $\mathrm{C}_*(u)$ (or identically $\mathrm{C}_*(\lambda)$) is the modulus of the intrinsic visibility of the partly resolved stellar component at the considered spatial frequency. Here, the visibility and the fringes phase are the modulus and the argument of $\hat{I}(\boldsymbol{w}, \lambda)$, respectively. In the approximation of a faint planetary companion where the flux ratio between the planet and the star is about several 10^{-3} in the N band, the visibility and the interferometric phase, defined with an unknown constant k, can be simplified to the first-order:

$$V_{\rm obj}(\lambda) \approx 1 - \frac{I_{\rm planet}(\lambda)}{\mathrm{C}_*(u) I_{\rm star}(\lambda)} \left[1 - \frac{1}{2}\cos(2\pi \boldsymbol{u}\cdot\boldsymbol{\rho})\right] \quad (3)$$

$$\Phi_{\rm obj}(\lambda) \approx \frac{I_{\rm planet}(\lambda)}{\mathrm{C}_*(u) I_{\rm star}(\lambda)} \sin(2\pi \boldsymbol{u}\cdot\boldsymbol{\rho}) + k. \quad (4)$$

As the phase cannot be measured without any reference, we use the possibility offered by both MIDI and AMBER instruments to

measure the relative phase between each of the channels of the spectrally dispersed fringes. The reference phase is usually taken as the average phase over all the channels. Then this gives access to the colour-differential phase, without the unknown constant k that disappears in the colour difference. The same process can be followed for obtaining the differential visibility.

In principle, the visibility and the phase carry complementary physical information, and both might be used for detecting and characterizing extrasolar planets. The fundamental noise sources affect the differential visibility and phase in a similar way, in contrast to the dispersion effects. The variations in the achromatic and chromatic OPD terms are more easily calibrated using the phase, since it has a linear dependence on OPD. This is not the case for visibility that has a quadratic dependence and is consequently much less affected, especially in differential mode. This constitutes a disadvantage since we want to estimate the amplitude of the dispersion effects on the OPD. A consequence is that some particular calibration tools allow us to correct the AMBER phase from systematic instrumental effects and not the visibility (Vannier et al. 2006). The closure phase could be also considered in parallel and would provide an observable that is free of any atmospheric and dispersion effects; however, it is not available for a two-telescope interferometer such as MIDI, so we instead focus on the differential phase.

2.3. Assumptions on the astrophysical source

The modelling of the flux of an irradiated planet requires careful attention on the radiative transfer conditions related to the stellar irradiation. Adressing this issue, Barman et al. (2001) modelled cool and hot irradiated 1-Jupiter mass and radius EGPs with intrinsic temperatures of 500 K and 1000 K, and various orbital distances. Regarding the atmospheric composition, especially in terms of opacity, two types of atmosphere were considered: a "dusty" atmosphere where all the particles and grains (mainly silicates) remain in the upper atmosphere, and a "condensed" one where dust has been removed from the upper atmosphere by condensation and gravitational settling. In order to conveniently model the Gliese 86b spectrum, different physical assumptions have to be considered.

The intrinsic temperature is the first discriminating parameter of the synthetic spectra. Because Gliese 86 is a few billion years old main-sequence star, its planetary companion can be considered as a fairly old planet that has undergone significant intrinsic cooling since its formation, regardless of any stellar irradiation (Guillot et al. 1996). Thus, an intrinsic temperature of 500 K seems more relevant for modelling Gliese 86b. Since we address the case of an irradiated planet, the atmosphere type and the opacity sources are essential and constitutes the second discriminating parameter. For our concern, we considered only the "condensed" model of Barman et al. (2001) since it seems more realistic for the substellar objects of weak temperature than the "dusty" one (Chabrier & Baraffe 2000).

Because it is required for calculating the theroretical planetary flux received on Earth, the issue of the planetary radius has to be carefully addressed in the irradiated case. According to theory (Saumon et al. 1996), isolated extrasolar giant planets shrink rapidly. In contrast, at small orbital separations, the evolution of an irradiated planet and of its radius are substantially slowed down by stellar heating (Burrows et al. 2000; Guillot et al. 1996). Therefore, to determine the theoretical radius of Gliese 86b, we used a mass-radius relation for irradiated planets, obtained from Guillot (2005). It considered various parameters involved in the definition of the cooling timescale and the temperature profile of the atmosphere. These parameters include the 1-bar temperature, the atmospheric composition, the opacity sources and the presence of clouds. Considering a 1-bar temperature of 1500 K for Gliese 86b, according to the theoretical values found in Barman et al. (2001), and a mass ranging from 4 to 13 $M_{\rm Jupiter}$, the corresponding radius of Gliese 86b would range from 1.05 to 1.2 $R_{\rm jup}$.

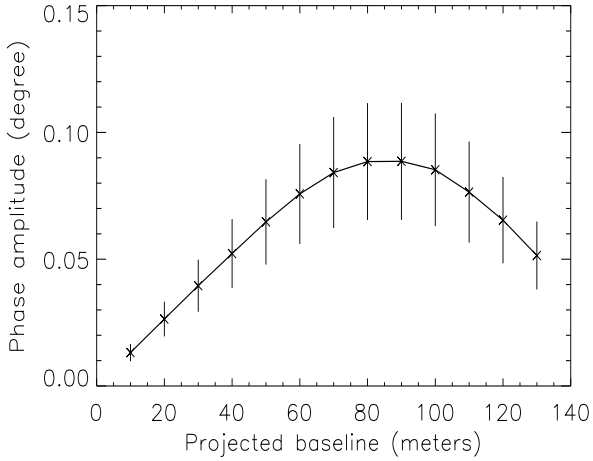

Fig. 2. Mean phase amplitude produced by Gliese 86b over the N band as a function of different values of baseline projected onto the separation vector ρ of the planetary system. Each amplitude value and "error" bar corresponds, respectively, to the mean and the standard deviation of phase amplitudes obtained with different planetary radii ranging from 1 to 1.4 $R_{\rm jupiter}$.

From an updated version of the 2001 synthetic spectra, Barman (private communication) has thus provided us with a synthetic spectrum of Gliese 86b following the physical assumptions described above, and the orbital features already determined by radial velocimetry. Since this synthetic spectrum corresponds to the flux at the surface of the planet, we needed to scale it by a dilution factor, implying the planetary radius, for getting $I_{\rm planet}(\lambda)$. A range of radii wider than the theoretical assumptions, from 1 to 1.4 $R_{\rm jupiter}$, has been considered here. Concerning $I_{\rm star}(\lambda)$, a simple blackbody law of emission was used with the effective temperature of Gliese 86, which we considered to be equal to about 5200 K (Flynn & Morell 1997; Butler et al. 2006).

2.4. Geometric parameters and resulting phase signal

Given that Gliese 86b was discovered by radial velocimetry, the inclination and position angles of the binary system in the plane of the sky are unknown. As a consequence, in the expression of the theoretical phase, the value of the projected baseline $B_{\rm proj}$ resulting from the scalar product $\boldsymbol{B}\cdot\boldsymbol{\rho} = B_{\rm proj}|\boldsymbol{\rho}|$ is also unknown. We thus consider a wide range of projected baselines from 10 to 130 m to calculate the theoretical signal.

As an example, the interferometric phase is calculated in Fig. 1 for a projected baseline value of 110 m (assuming a 130 m baseline at ground level) and for a mean planetary radius equal to 1.2 $R_{\rm jupiter}$. We see that in N band (8 to 13 μm), the signal is quite linear because of the partially resolved separation between star and planet, and its corresponding amplitude is close to 0.1°. The "phase amplitude" is defined as the difference between the highest and lowest values over the N band of the interferometric phase.

In Fig. 2, the evolution of the phase amplitude over the N band is displayed as a function of the projected baseline. It

appears that for most values of projected baseline, the mean phase amplitude is greater than 0.05°. In addition, the maximum phase amplitude, equal on average to 0.9°, does not occur for the 130 m baseline but instead for the shorter 90 m baseline. The reason is that, while large projected baseline values imply normally large phase amplitude because of the higher angular resolution, the phase amplitude also depends on the evolution of the sine modulation period as a function of wavelength (see Eq. (4)). A 0.05° level of precision on the phase measurement would allow us to achieve the phase signal of the planet for a large set of projected baseline values, ranging from 50 to 130 m.

3. Dispersion and correction of the phase signal

3.1. Effects of dispersion

The incoming wavefronts collected by each telescope are affected by different pertubations during their propagation through the atmosphere and the instrument. Most of the perturbations affecting independently each wavefront are corrected by an adaptive optics device. Then for single mode spatial-filtered instrument such as MIDI, the residual wavefront perturbations are eventually limited to an optical path difference (OPD) between the two beams. This implies a degradation of the interferometric observables and especially the phase, since a perturbating term is added to the intrinsic phase signature of the science source. The causes producing such a pertubating OPD are

- use of the air-filled delay lines to correct an astronomical differential path delay occurring in the vacuum, a contribution that can be seen as a quasi-static OPD component.
- other causes such as the refractive index fluctuations of free atmosphere and air inside interferometric tunnels, a contribution that can be seen as a variable OPD component as a function of time.

The expression of this "dispersive" phase is

$$\Phi_{\rm disp}(\lambda, t) = \frac{2\pi}{\lambda}\,{\rm OPD}(\lambda, t). \tag{5}$$

The dispersion relations and their effect on stellar interferometry can be found under a detailed form in Tango (1990) and Davis et al. (1998). To address the problem of the dispersion caused by the air, the atmospheric refractivity included in the expression of the OPD can be written as a sum over atmospheric constituents by approximating the Lorentz-Lorenz relation, to yield

$$N(\lambda) = n(\lambda) - 1 \approx \sum_{\rm s} R_{\rm s}(\lambda)\,\varrho_s, \tag{6}$$

where $R_{\rm s}(\lambda)$ is the specific refractivity calculated from the various absorption resonances of the considered constituent, and $\varrho_{\rm s}$ is the partial density. Following the approach of Colavita et al. (2004), it is convenient to write this as a sum of the main atmospheric contributors that is, dry air and water vapour:

$$N(\lambda) \approx N_{\rm da}(\lambda) + N_{\rm wv}(\lambda) = R_{\rm da}(\lambda)\,\varrho_{\rm da} + R_{\rm wv}(\lambda)\,\varrho_{\rm wv}, \tag{7}$$

which yields

$$\Phi_{\rm disp}(\lambda, t) = \frac{2\pi}{\lambda}\,{\rm OPD}_{\rm da}(\lambda, t) + \frac{2\pi}{\lambda}\,{\rm OPD}_{\rm wv}(\lambda, t). \tag{8}$$

According to the first paragraph of this section, an OPD term is caused either by a geometric path difference (quasi-static contribution) or by a refractive index fluctuation (variable contribution). Considering water vapour, the general expression expliciting these contributions is

$$\begin{aligned}{\rm OPD}_{\rm wv}(\lambda, t) &= \frac{2\pi}{\lambda}\,N_{\rm wv}(\lambda)\,\delta L + \frac{2\pi}{\lambda}\,\delta N_{\rm wv}(\lambda, t)\,L_{\rm tot}\\ &= \frac{2\pi}{\lambda}\,R_{\rm wv}(\lambda)\,\varrho_{\rm wv}\,\delta L + \frac{2\pi}{\lambda}\,R_{\rm wv}(\lambda)\,\delta\varrho_{\rm wv}(t)\,L_{\rm tot}. \end{aligned}\tag{9}$$

The expression is the same for dry air. The "quasi-static" contribution corresponds to the common situation where an astrophysical object is observed at a projected zenith distance $Z_{\rm p}$. An excess air path is thus covered by one beam when delay lines are used to correct an astronomical path difference in the vacuum denoted as $\delta L = B\sin(Z_{\rm p})$. The symbol $\varrho_{\rm s}$ represents the mean density conditions of the atmospheric component (dry air or water vapour) inside the tunnels.

The "variable" contribution highlights that, even though both beams cover an equal geometrical path from the top of the atmosphere to the recombining device ($L_{\rm tot}$), differential density fluctuations of the atmospheric component between each path, $\delta\varrho_s(t)$, will introduce an OPD. These fluctuations depend on the temperature, pressure, and humidity differences between the paths of the beams, consequently on time.

The terms ${\rm OPD}_{\rm da}(\lambda, t)$ and ${\rm OPD}_{\rm wv}(\lambda, t)$ contain a dominant achromatic term corresponding to the uncorrected achromatic delay or "piston" between beams, and a chromatic term representing the higher order dispersion. The piston is equal to the mean slope of the linear component of the phase as a function of the wavenumber $k = \frac{2\pi}{\lambda}$. In mathematical terms, this piston corresponds to the zero-order term of ${\rm d}\Phi_{\rm disp}(k)/{\rm d}k$, that is to say, the group delay as defined in Meisner & Le Poole (2003) or Colavita et al. (2004). This linear part of the "dispersive" phase will affect the measurements by adding to the linear part of the planetary signal.

By explicitly calculating the "achromatic" and "chromatic" dispersion terms for each atmospheric component, the total dispersive phase can be formulated as

$$\begin{aligned}\Phi_{\rm disp}(\lambda, t) &= \frac{2\pi}{\lambda}D_{\rm g} + \Phi_0 + \frac{2\pi}{\lambda}{\rm OPD}_{\rm da}(\lambda, t)\\ &\quad + \frac{2\pi}{\lambda}{\rm OPD}_{\rm wv}(\lambda, t).\end{aligned}\tag{10}$$

Here, $D_{\rm g}$ represents the total piston of both OPD terms of Eq. (8), and Φ_0 the origin phase. Now, ${\rm OPD}_{\rm da}(\lambda)$ and ${\rm OPD}_{\rm wv}(\lambda)$ contain only the chromatic part, i.e. the higher order dispersion. In mathematical terms, these two OPD terms contain the remaining higher order terms of the group delay or, in an equivalent manner, of the phase delay (defined as $\Phi_{\rm disp}(k)/k$).

In terms of data processing, where the different contributions producing a dispersive phase are generally removed by a fitting procedure, it is convenient to make ${\rm OPD}_{\rm da}$ and ${\rm OPD}_{\rm wv}$ explicit as a function of one single parameter, $f_{\rm da}(t)$ and $f_{\rm wv}(t)$ respectively, containing all the contributions that affects the dispersion amplitude:

$$\begin{aligned}\Phi_{\rm disp}(\lambda, t) &= \frac{2\pi}{\lambda}D_{\rm g} + \Phi_0 + \frac{2\pi}{\lambda}R_{\rm da}(\lambda)[\varrho_{\rm da}\delta L + \delta\varrho_{\rm da}(t)L_{\rm tot}]\\ &\quad + \frac{2\pi}{\lambda}R_{\rm wv}(\lambda)[\varrho_{\rm wv}\delta L + \delta\varrho_{\rm wv}(t)L_{\rm tot}]\\ &= \frac{2\pi}{\lambda}D_{\rm g} + \Phi_0 + \frac{2\pi}{\lambda}R_{\rm da}(\lambda)f_{\rm da}(t) + \frac{2\pi}{\lambda}R_{\rm wv}(\lambda)f_{\rm wv}(t).\end{aligned}\tag{11}$$

The behaviour of dry and humid refractivity laws is different according the spectral band. The empirical humid law is

very sloping in the mid-infrared and very flat in the near infrared, whereas it is the opposite for the theoretical dry air law. Therefore in the N band, the dispersion introduced by the propagation through the air is dominated by its humid component (Meisner & Le Poole 2003; Meisner et al. 2004), and the dispersive phase affecting the MIDI data becomes

$$\Phi_{\mathrm{disp,wv}}(\lambda, t) = \frac{2\pi}{\lambda} D_g + \Phi_0 + \frac{2\pi}{\lambda} R_{\mathrm{wv}}(\lambda) f_{\mathrm{wv}}(t). \quad (12)$$

Other terms affect the interferometric phase measurements, such as the fundamental noise or the instrumental phase. They are discussed in the following section.

3.2. Mono-band observations

In mono-band interferometric observations, the correction of the different terms of the dispersive phase is performed by fitting the measured interferometric phase over the spectral range of the band with refractive index models of dry air and water vapour. The first contribution of the dispersive phase to be removed from measurements is the dominant linear part. A linear fit on the total interferometric phase is performed to estimate and remove the mean slope, that is to say, the "D_{g}" term detailed in Sect. 3.1. Unfortunately, by doing so, we also remove any linear trend due to the planet signal.

Once this contribution has been removed, the phase is constituted by the non-linear contribution of the dispersion along with the remaining planet signal, both having a curvature-like or quadratic aspect. The amplitude of the curvature introduced by the non-linear dispersion term can typically reach about 10° (Meisner et al. 2004) and overwhelm the curvature due to the planet. For the sake of detection, an additional correction is thus required.

A fit of the phase curvature, by estimating $f_{\mathrm{wv}}(t)$ and $f_{\mathrm{da}}(t)$ from a model of refractivity, would allow removal of the 2nd order contribution of the dispersive phase. However, the curvature-like part of the planetary signal would be removed at the same time, letting an even smaller phase signature from the planet.

As previously mentioned, two other terms affect the differential phase measurements, the instrumental and fundamental noise terms. For MIDI, the instrumental term can in principle be calibrated by a nearby star observed close in time to the target star. A device called BCD (for beam commutator device) allows us to quickly and accurately calibrate the instrumental phase of AMBER. Concerning the fundamental noises, they represent the sources of noise that cannot be reduced for a given instrumental setup. In the N band, where the thermal background is the principal source of fundamental noise, an empirical law gives the expected value for the relative error on phase assuming that MIDI is used with photometric channels:

$$\sigma_\Phi \approx \frac{1}{0.4 \times 10^{(5-m_{\mathrm{N}})/2.5}} \times 0.105 \sqrt{\frac{n_{\mathrm{ch}}}{T/0.1}}, \quad (13)$$

with n_{ch} the number of independent spectral channels, T the integration time in seconds, and m_{N} the stellar magnitude in N band.

3.3. Multi-band observations

For astrophysical sources such as close-in EGPs, the differential phase has a strong chromatic dependence. The exoplanet signature may be negligible, that is, below the fundamental noise level in one spectral band and significant in another band. A "multi-band" approach is thus applicable to correct the water vapour dispersion. Colavita et al. (2004) addresses this issue in the context of the standard phase referencing. By using a phase reference in K band, they estimate that 59% of the water vapour's seeing effects would remain uncompensated in N band, because of the higher chromatic "sensitivity" of the humid dispersion law. However, these results do not apply to our approach in which fringes were independently and simultaneously obtained in both bands. As explained, the "reference phase" in K band is not used here as a first-order tracking of the fringes in N band (science band), but rather as an estimate of the instantaneous amplitude of the water vapour dispersion.

In a single band observation, we saw that the estimation of the dispersion effects takes not only the "true" amplitude of dispersion into account, but also the "dispersion-like" part of the planetary signal. In contrast, by simultaneously observing in a band where the astrophysical signal is negligible, we should be able to directly estimate the true amplitudes of dispersion represented by the achromatic factors, $f_{\mathrm{da}}(t)$ and $f_{\mathrm{wv}}(t)$, without any additional significative phase signal coming from the source. Then an extrapolation of these achromatic factors to the spectral band of interest would allow correction of only the non-linear dispersive component of the phase without affecting the remaining object signal.

In our case, that is MIDI observing in N band and AMBER observing in K band, the parameter of interest to extrapolate is $f_{\mathrm{wv}}(t)$. Nevertheless, the precision on the estimates of this parameter depends on the data quality, and in some cases a degeneracy between $f_{\mathrm{da}}(t)$ and $f_{\mathrm{wv}}(t)$ may occur in the fit. In a general way, if the differential phase in K band is degraded and deviates from the typical water vapour dispersion pattern, the estimation of the achromatic factor representing the dispersion amplitude is affected by an error denoted hereafter as $\delta f_{\mathrm{wv}}(t)$. According to Eq. (12) and assuming that the linear part has been removed, the corresponding error on the estimation of the de-pistoned dispersive phase affecting the other band is

$$\delta\Phi_{\mathrm{disp,wv}}(\lambda, t) = \Phi_{\mathrm{disp,wv}}(\lambda, t) \, \frac{\delta f_{\mathrm{wv}}(t)}{f_{\mathrm{wv}}(t)} \, . \quad (14)$$

More precisely, this expression corresponds to the accuracy with which the N band differential phase could be corrected from the 2nd order water vapour dispersion, using the parameter $f_{\mathrm{wv}}(t)$ (estimated in K band).

In parallel, we compared the relative slopes of the tabulated water vapour dispersion law on the extent of the K and N band, as shown in Colavita et al. (2004) or Mathar (2004). The chromatic sensitivity of the water vapour refractivity appears to be two times greater in N band than in K band. It thus implies that, for a same dispersion amplitude f_{wv}, the corresponding curvature of the de-pistoned dispersive phase is about two times greater in N than in K band. Therefore, it is essential to get precise differential phase measurements in K band, hence precise measurements of $f_{\mathrm{wv}}(t)$, in order to limit the propagation of the error when applying this achromatic factor to the N band.

For example, we plotted in Fig. 3 the relative error on the wet dispersion parameter f_{wv} with respect to the standard deviation, per spectral channel, of a Gaussian error that would affect a dispersive phase calculated from a standard humid dispersion law in K band (in radians). According to the grey curve in Fig. 3, this shows that a typical error of 0.01 radians on the phase measurement in K band implies a relative error of 5% on the wet dispersion parameter. According to Eq. (14), if the water vapour dispersion introduces, for example, a curvature amplitude of 5° in N band, the calibration accuracy would be $\delta\Phi_{\mathrm{disp,wv}}(\lambda) = 0.25°$. With such a corrected N band differential

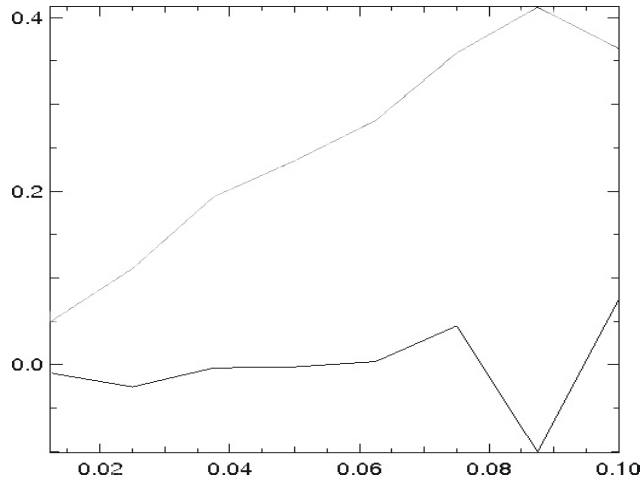

Fig. 3. Relative error on wet dispersion parameter (black: average; grey: rms) as a function of a Gaussian error per spectral channel affecting a theoretical dispersive phase in K band. The error on the K band phase is expressed in radians, and 12 spectral channels are considered.

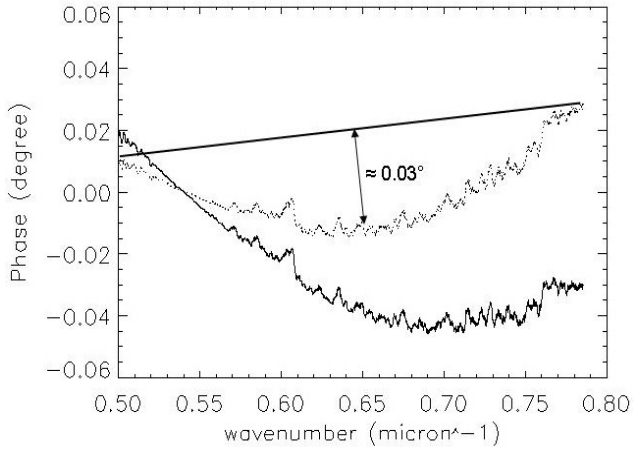

Fig. 4. Example of the expected amplitude of the planet signal as a function of wavenumber (k) in N band. In this example, we consider a projected baseline of 110 m, and a planetary radius of 1.2 $R_{\rm jupiter}$. The solid line curve corresponds to the total theoretical phase, while the dotted line one corresponds to the theoretical phase after fitting out the linear part. The vertical arrow represents the approximative expected amplitude of that "de-pistoned" phase.

phase, we would stand at a factor of about 10 above the phase signal of Gliese 86b.

3.4. Actual required level of precision

As discussed in Sect. 3.2, the first-order correction of dispersion effects will remove any linear contribution in the interferometric phase, which also includes the linear part of the object phase. Therefore the actual phase amplitude has to be evaluated on an "de-pistoned" interferometric phase.

In the case of a 110 m baseline and a 1.2 $R_{\rm jupiter}$ planetary radius, we see in Fig. 4 that the remaining planetary phase signal (or "de-pistoned" phase) is a curvature-like function of the wavelength (or wavenumber) in N-band. The amplitude of this signal is consequently lower and approximately equal to 0.03° instead of 0.08°.

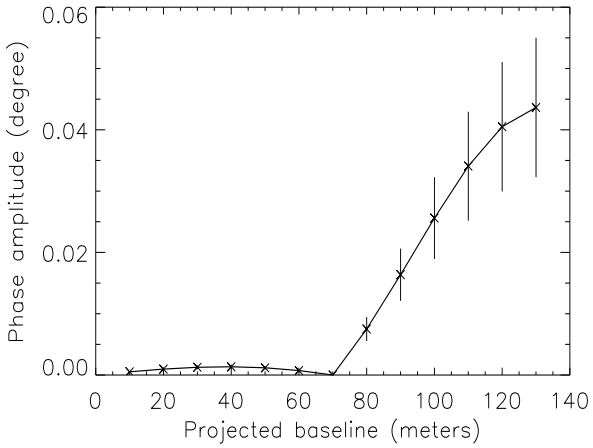

Fig. 5. Amplitude of the "de-pistoned" Gliese 86b interferometric phase over the N band as a function of different values of baseline projected onto the separation vector ρ of the planetary system. Each amplitude value and "error" bar correspond respectively to the mean and the standard deviation of phase amplitudes obtained with different planetary radii ranging from 1 to 1.4 $R_{\rm jupiter}$.

In Fig. 5, we represent the evolution of the amplitude of the "de-pistoned" phase over the N band as a function of the projected baseline.

The curvature substantially varies with the projected baseline and is at its maximum for the 130 m baseline (≈0.05°), whereas it is close to zero for projected baselines lower than 70 m where the phase has a strong linear trend. It happens that if the source is observed with a projected baseline greater than or equal to 100 m, a precision of about 0.03° on the phase measurement would be enough to achieve the level of the phase signature from the planet. As a conclusion it seems clear that, considering de-pistoned phases, the required precision is lower and the range of projected baselines allowing this astrophysical signal level is more limited.

4. Experience

4.1. Technical scheme of simultaneous observations

For the first time, the instruments MIDI (in the N-band, 8−13 μm) and AMBER (in the near-IR 1−2.4 μm) were simultaneously used for the observation of Gliese 86. In Fig. 6, we represent the simplified optical path of AMBER and MIDI in the VLTI laboratory. We chose to set MIDI as the master instrument for the VLTI subsystems, while AMBER was running in a stand-alone mode. The simultaneous use of the two instruments implies, in principle, that they have similar transversal alignment, longitudinal alignment, and temporal synchronicity. In practice, each of these adjustments has only been approximated, as best as possible.

Because AMBER is more stringent in terms of transversal alignment (because of the shorter wavelength and the use of a fiber spatial filter), the global pointing offsets used for that alignment were found by optimizing the fiber injection on AMBER. Due to a slight non-alignment between the two instruments, this optimization on AMBER resulted for MIDI in a 2-pixel shift in the telescopes beam overlap, although the standard tolerance for the overlap shift is in principle 0.8 pixels. Nevertheless, the overlap quality was still good enough to produce fringes with the aim of measuring differential phases on the target (1-Jy at 12 μm correlated flux). Moreover, this

Table 1. Log of the observing sequences (left table: November 17 2007; right table: November 24 2007).

Object	Time (UT)	$B\cos(Z_p)$ (m)	$B\sin(Z_p)$ (m)
HD 9362	00h05min	129.6	–12.9
HD 9362	00h11min	129.7	–11.5
HD 9362	00h22min	129.9	–8.6
HD 9362	00h31min	130.0	–6.6
HD 9362	00h40min	130.1	–4.3
HD 9362	00h48min	130.2	–2.3
HD 9362	00h57min	130.2	–0.3
GL 86	02h13min	129.5	13.2
GL 86	02h18min	129.4	14.5
GL 86	02h26min	129.1	16.7
GL 86	02h33min	128.8	18.9
GL 86	02h40min	128.5	21.2
HD 12524	03h02min	127.8	24.6
HD 12524	03h10min	127.3	27.3
GL 86	03h32min	124.7	37.5
GL 86	03h41min	123.8	40.2
HD 12524	03h59min	121.1	47.8
GL 86	04h15min	119.8	51.1
GL 86	04h22min	118.7	53.4

Object	Time (UT)	$B\cos(Z_p)$ (m)	$B\sin(Z_p)$ (m)
HD 9362	00h00min	130.0	–7.5
HD 9362	00h15min	130.1	–3.8
HD 9362	00h28min	130.2	0.5
GL 86	01h04min	130.2	1.7
HD 12524	01h36min	130.1	4.7
HD 9362	01h52min	127.8	24.9
GL 86	02h05min	128.8	18.9
GL 86	02h24min	127.8	24.7
GL 86	02h42min	126.6	30.4
HD 12524	02h56min	126.1	32.4
GL 86	03h28min	122.2	45.0
GL 86	03h33min	121.6	46.6
GL 86	03h44min	120.2	50.1
GL 86	03h52min	119.2	52.5
GL 86	04h00min	117.9	55.1

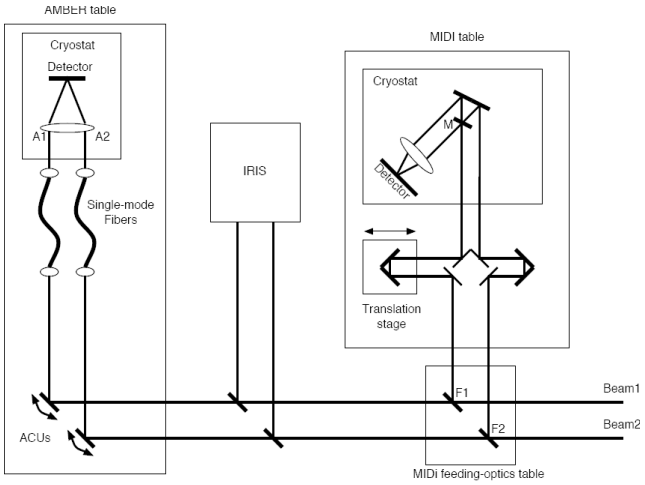

Fig. 6. Simplified optical path of AMBER and MIDI in the VLTI laboratory, highlighting the important elements to be considered for parallel operation.

misalignment prevented us from extracting well-calibrated visibility curves.

For the longitudinal alignment, the fringe optimization was also first performed on AMBER, by moving the external VLTI delay lines. It was then necessary to correct the optical path difference offset between AMBER and MIDI (measured on a bright target at the beginning of each night before the observations) by moving the internal delay lines of MIDI up to a value δ_{am} corresponding to the fringe optimization of MIDI. During the observation, the fringe tracking was performed by MIDI, which can send corrections to the VLTI OPD controller. Therefore the fringes were not stabilized on AMBER, with a residual OPD of about 10 μm. As FINITO was not used, the expected data quality of AMBER was the one obtained when AMBER works alone with a correct estimation of the baseline vector and under good seeing. The main limitation of this longitudinal alignment procedure was the chromatic dependence of the OPD offset δ_{am}. As a result of that effect, the AMBER fringes, initially positioned vertically, started to be significantly tilted after a few hours of observation (i.e. when the change in the projected baseline of the target induced a significant differential OPD in K band).

4.2. Sequence of the observations

These simultaneous observations were carried out on 2007 November 17 and 24 with the UT1-UT4 baseline during five hours (from 00:00 UT to 04:30 UT, approximately). According to the predicted ephemerides of the system, this interval of one week would correspond to both maxima for the angular separation between star and planet, putting the planet on one side of the star and then on the other.

Moreover, we tried to observe close to the plane perpendicular to the baseline (plane corresponding to the zero delay position of the delay lines) in order to minimize the air asymmetry into the interferometric tunnels as much as possible. Also, the observation of the source at opposite positions before and after the zero delay crossing could be used for calibrating the chromatic dispersion within the delay lines using only MIDI. The consequent switch of the OPD sign would imply an inversion of the slope of the differential phases measured at opposite positions before and after the zero delay crossing. Then a simple subtraction would allow removal of the dispersive contribution due to the air asymmetry within the delay lines. If the amplitude of the atmospheric dispersion is greater than the contribution of the dispersion within the delay lines, this method is no longer usable. Moreover, this method requires very good timing on the observing sequence.

In order to test this possibility of calibration, in addition to the main calibration procedure using AMBER and MIDI, we considered it in the preparation of the observing sequence of each night. The zero delay crossing and the use of the consequent switch of the OPD sign were attempted for the target and two calibrators, HD 9362 and HD 12524, which were observed alternately as shown in Table 1. Unfortunately, some problems of coordinates and proper motion correction for Gliese 86 disordered the prepared observing sequence for both nights, during the telescope pointing and the acquisition on IRIS.

Despite all of that, fringes were detected for the three objects. For example, concerning the "master" instrument MIDI, for the first night, nine fringe exposures were obtained for Gliese 86,

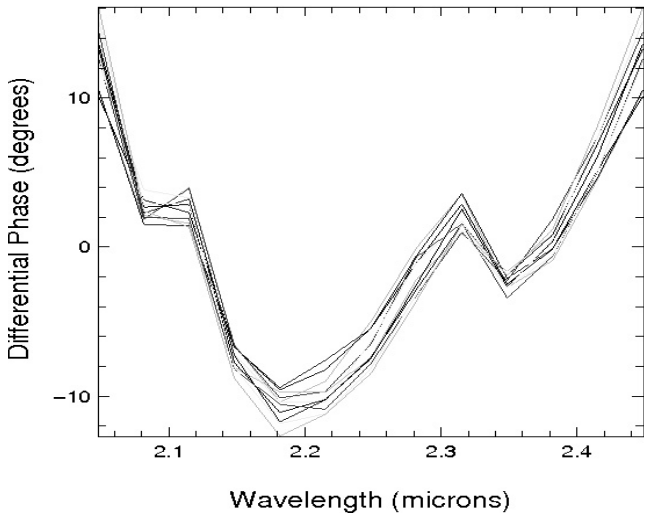

Fig. 7. Differential phases of Gliese 86 observed with AMBER on 2007 November 17, for a time sequence of about 12 min. Each curve corresponds to a phase that is auto-calibrated from instrumental internal effects using the BCD, and the average slope is subtracted.

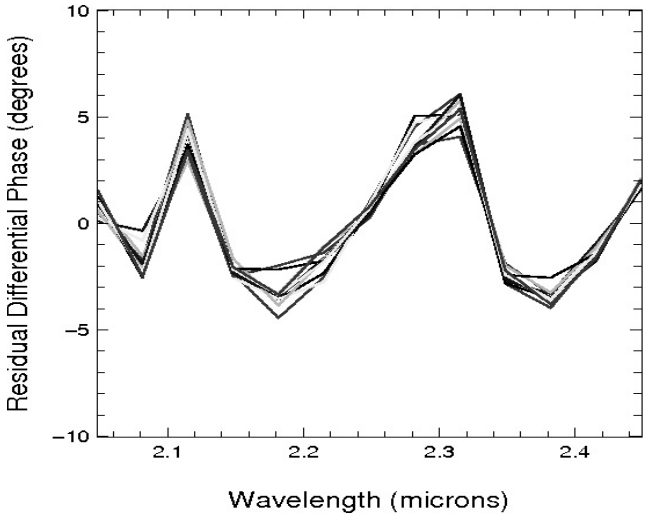

Fig. 8. Residual of the AMBER differential phases presented in Fig. 7 after individual fits of the wet and dry chromatic dispersion laws.

seven for HD 9362, and three for HD 12524. For the second one, we also did nine fringe exposures for Gliese 86, four for HD 9362, and two for HD 12524.

However, because of the changes in the prepared observing sequences, we were only able to observe the first calibrator (HD 9362) before and after the zero delay crossing. Although the slope inversion due to the switch of the OPD sign was visible for two opposite phase measurements, the method was not really usable given the greater amplitude of the atmospheric dispersion during most of the observations and given the disordered observing sequence.

5. Results

5.1. Precision reached on the extrapolation with AMBER data

The simultaneous observation with the two VLTI instruments was a success and fringes were obtained with AMBER while MIDI was guiding. Due to technical compromizes for the longitudinal alignment, the MIDI data were degraded giving a non-optimum quality and a poor SNR on the differential phase.

The quality of the fringes observed with AMBER varies largely depending on the observing conditions and on the quality of the beam injection. In Fig. 7, we present the differential phases from a "good" sequence, after de-pistoning and subtraction of internal instrumental effects using an autocalibration by a BCD. The statistical dispersion between the curves over that 12 min sequence is about 1 degree rms, on average. The plot shows a fairly stable rough pattern, which is even more obvious when looking at the residual after fitting the phase curves individually with the wet and dry chromatic dispersion laws (Fig. 8). The fit residuals are roughly stationary and show a statistical dispersion of about 0.4 degree rms that is compatible with a normal distribution around the average curve. The average pattern, showing sine-like waves, is believed to originate from a parasitic Fabry-Perot effect in the AMBER polarizers (replaced since). An additional piston effect probably affected the AMBER observations, whose quality is significantly poorer in other sequences, since the tracking of AMBER fringes was performed with MIDI without using FINITO. Fringes were not stabilized by the fringe tracking of MIDI, and this is particularly sensitive because of the UTs. The consequence of these degradations was a loss of correlated flux, therefore a loss of SNR on the phase.

From Monte-Carlo simulations of the fit of noisy simulated data, we previously deduced a relationship between the precision on the retrieved dispersion parameters and the standard deviation in the noise on the differential phase. The observed scatter on the AMBER residual phase presented in Fig. 8, whose statistics are consistent with our simulations, can then be related to a relative error on the wet dispersion parameter. For the sequence presented above, that error is about 2.5%.

According to Eq. (14) and knowing that $\frac{\delta f_{\rm wv}(t)}{f_{\rm wv}(t)} \approx 2.5\%$, we can deduce the correction accuracy of the dispersive phase affecting the MIDI data, namely $\delta\Phi_{\rm disp,wv}(\lambda)$. For that we evaluate the amplitude of $\Phi_{\rm disp,wv}(\lambda)$, which is the curvature amplitude affecting the MIDI differential phases during the same sequence as the one considered for AMBER. Unfortunately, because of the strong loss of SNR affecting the MIDI data, the differential phases of Gliese 86 obtained during this observing sequence were too noisy to clearly distinguish the typical curvature-like wet dispersion pattern. Instead, we used the first phase measurement of the second bright calibrator HD 12524, obtained just after the end of the first observing sequence of Gliese 86. At this time, both objects were observed with similar airmasses and $B\sin(Z_{\rm p})$ values (see Fig. 1), therefore the curvature observed on the differential phase of HD 12524 should give a fairly good estimation of the amplitude of the dispersive phase that affected the first sequence of Gliese 86 phase measurements.

By fitting the differential phase of HD 12524 with the tabulated water vapour dispersion law taken from Mathar (2004), we estimated a curvature amplitude of about 13°, which gives $\delta\Phi_{\rm disp,wv}(\lambda) \approx 0.3°$. With such a calibration accuracy for MIDI differential phases, we finally arrive at a factor of 10 above the phase signature from the planet Gliese 86b (≈0.03°).

5.2. Precision reached on MIDI curvature measurements

As discussed above, the phase signature from Gliese 86b is about 0.03° and thus implies a high precision measurement of the phase curvature. By using the MIDI data alone, we have no means to estimate and correct the dispersion due to water vapour in a satisfactory way. For example, a fit of the Gliese 86 phase

using the refraction index model of Mathar would remove the dispersion but also the curvature due to the planet. Also the calibration by reference star to correct this dispersion is not relevant given the evolution time of the "non-turbulent" fluctuations of water vapour, which is shorter than the time interval between the observation of the source and the calibrator.

Because the AMBER data is unusable for the extrapolation and correction of the wet dispersion, we focus on the possibility of estimating the level of precision of the curvature measurement that we could achieve with the MIDI data. This can be done by correcting the instrumental and atmospheric effects as much as possible on the phases of a calibrator and after estimating a curvature on the residual phases. The reason is that a calibrator is generally an unresolved star with an intrinsic phase equal to zero.

In our case we considered the data of the calibrator HD 9362 taken during the first night. The estimation of the standard deviation of the curvature measurements between the phases of various exposures (7 for HD 9362) can give the general precision that we could achieve.

The method of estimation consists in several steps:

- The mean of all the measured differential phases is subtracted from each differential phase (produced by each fringe exposure) noted $\Phi_i(\lambda)$:

$$\Phi'_i(\lambda) = \Phi_i(\lambda) - \frac{1}{7}\sum_{i=1}^{7}\Phi_i(\lambda). \quad (15)$$

  The data reduction software that we used here, named EWS, allows us to check that phases are not wrapped (Jaffe 2004). This calibration removes a large part of phase trends that could be caused by instrumental and other invariable effects during the night, such as a large part of the ozone absorption signature at 9.6 μm.
- Then we use the refractive index model of Mathar to fit and remove the variable water vapour dispersion not suppressed by the first step:

$$\Phi''_i(\lambda) = \Phi'_i(\lambda) - \mathrm{fit}_{\mathrm{Mathar}}(\Phi'_i(\lambda)). \quad (16)$$

  From that point, the residual noise only remains in the curvature of the phase.
- A 2nd order polynomial fit is applied to each of the residual phases ($\Phi''_i(\lambda)$) for revealing the residual curvature.
- The residual curvature can be directly estimated by calculating the second difference between three values of the polynomial fit for each exposure: at 8 μm, at a wavelength located around the middle of the band, and at 13 μm. We note these values S_8, S_{mid}, and S_{13}, such that the second difference is

$$\text{2nd difference} = \frac{S_8 + S_{13} - 2 * S_{\mathrm{mid}}}{2}. \quad (17)$$

  It is important to note that we maximize the curvature estimation here since the wavelength corresponding to S_{mid} is chosen precisely to maximize the second difference.

In Fig. 9, we show the results of this curvature estimation for each exposure (set of data) during the night of November 17. The values of estimated curvature are not equal to zero, as we can expect, and vary from −0.4° to 0.45°. The estimated curvature is at zero-mean with a standard deviation of 0.33°. Due to the uncertainties on the fitted parameters and consequently on the estimation of the second difference, this standard deviation has an uncertainty of 0.05°.

This estimation of the dispersion of the second difference during the night means that we could not measure a curvature smaller than 0.33 ± 0.05°. This value stands at a factor 10 above the phase signal of Gliese 86b.

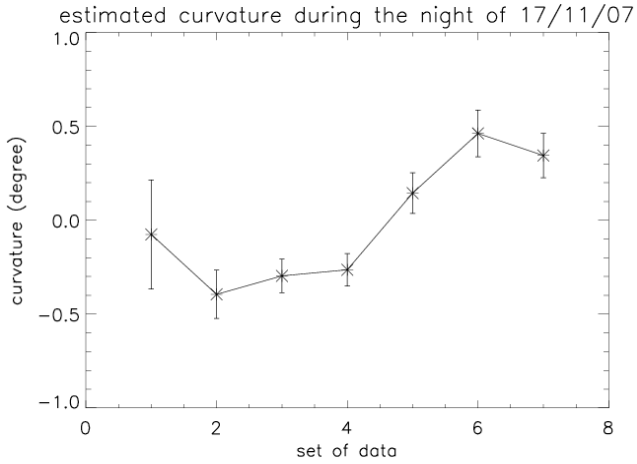

Fig. 9. Evolution of the estimated phase curvature for the calibrator HD 9362 as a function of the considered spectrum (or set of data). The number on the x-axis, giving the set of data, corresponds to the chronological order of measurements during the night.

6. Discussion and future improvements

Direct observation of close-in EGPs is currently one of the most challenging programmes for the MIDI instrument, the VLTI, and in general for ground-based long baseline interferometry. By considering the observing and data reduction process, a theoretical precision of the order of 0.03° on the phase would be required to detect the exoplanet Gliese 86b orbiting the K-dwarf star Gliese 86. From the data of our MIDI GTO observations of 2007 November, we estimated the smallest measurable curvature as equal to 0.33°. This value is still ten times higher than the theoretical requirements.

As a step towards potential detection, a more favourable source providing a stronger signal could become available since new targets have been discovered by radial velocimetry. In this case, a better resolved and, at the same time a warmer planet would be appropriate. Thanks to better resolution, we would have an almost complete sine modulation cycle all over the whole N band (see Fig. 1) and no longer a quasi-linear phase. It would thus imply a larger remaining phase amplitude due to the planet, after suppression of the piston.

In addition to the feasibility study accompanying this first attempt, we have shown that it is possible to carry out parallel observations of the same target with AMBER and MIDI. By using the fringes obtained in K-band, the aim was to correct the phase in N-band from the strong water vapour dispersion without removing the planet contribution. However, several technical constraints and problems degraded the AMBER data, so they were too noisy to be directly extrapolated. Nevertheless, in terms of calibration accuracy, we can infer that we approximately stand at a factor of 10 above the phase signature from the planet.

Different technical and observational improvements were made (two first items in the list) or could be envisaged to get better data quality for both instruments, consequently improving the chances of detection:

- Ability of AMBER to control its ACUs (atmospheric compensation units) in order to optimize the injected flux with the IRIS instrument offsets set for MIDI. Thanks to that the MIDI overlap will be much better for our experiment;

- Use of FINITO and fix of the polarizers on AMBER to obtain stabilized fringes on this instrument;
- Implementation of slight modifications in the AMBER and MIDI template sequence files (perspective of an AMBER+MIDI service mode) including the synchronization of the frames of MIDI and AMBER, and an automatic correction of the delay lines position at each preset;
- Use of a larger baseline to increase the angular resolution;
- Correction of the ozone absorption signature in the phase by the data reduction process.

In the future, MATISSE, a four-beam interferometer, will be the successor to MIDI and will include among others a pair-wise recombination and the simultaneous use of *L* and *N*-bands. In this framework, we expect the *L* band to be very favourable in terms of thermal background and instrumental stability, and the linear part of the phase signal to be measurable. As a consequence, the chances of exoplanet detection will be strongly improved.

Acknowledgements. We would like to thank the ESO staff of Paranal and Garching, especially Thomas Rivinius, Markus Schoeller, and Fredrik Rantakyro, for their collaboration that made this experiment possible. We also thank Travis Barman, from the Lowell observatory, for providing us with an updated synthetic spectrum corresponding to the Gliese 86b characteristics, along with the referee for his valuable comments that improved the paper.

References

Barman, T. S., Hauschildt, P. H., & Allard, F. 2001, ApJ, 556, 885
Burrows, A., Guillot, T., Hubbard, W. B., et al. 2000, ApJ, 534, L97
Butler, R. P., Wright, J. T., Marcy, G. W., et al. 2006, ApJ, 646, 505
Chabrier, G., & Baraffe, I. 2000, ARA&A, 38, 337
Colavita, M. M., Swain, M. R., Akeson, R. L., Koresko, C. D., & Hill, R. J. 2004, PASP, 116, 876
Davis, J., Tango, W. J., & Thorvaldson, E. D. 1998, AO, 37, 5132
Flynn, C., & Morell, O. 1997, MNRAS, 286, 617
Guillot, T. 2005, Annual Review of Earth and Planetary Sciences, 33, 493
Guillot, T., Burrows, A., Hubbard, W. B., Lunine, J. I., & Saumon, D. 1996, ApJ, 459, L35
Jaffe, W. J. 2004, in New Frontiers in Stellar Interferometry, ed. W. A. Traub, SPIE Conf., 5491, 715
Joergens, V., & Quirrenbach, A. 2004, in SPIE Conf. Ser. 5491, ed. W. A. Traub, 551
Leinert, C., Graser, U., Przygodda, F., et al. 2003, ApSS, 286, 73
Lopez, B., Petrov, R. G., & Vannier, M. 2000, in SPIE Conf. Ser. 4006, ed. P. Léna, & A. Quirrenbach, 407
Mathar, R. J. 2004, AO, 43, 928
Mayor, M., & Queloz, D. 1995, Nature, 378, 355
Meisner, J. A., & Le Poole, R. S. 2003, in SPIE Conf. Ser. 4838, ed. W. A. Traub, 609
Meisner, J. A., Tubbs, R. N., & Jaffe, W. J. 2004, in New Frontiers in Stellar Interferometry, ed. W. A. Traub, SPIE Conf., 5491, 725
Petrov, R. G., & Amber Consortium, T. 2003, in EAS Publ. Ser. 6, ed. G. Perrin, & F. Malbet, 111
Queloz, D., Mayor, M., Weber, L., et al. 2000, A&A, 354, 99
Richardson, L. J., Deming, D., Horning, K., Seager, S., & Harrington, J. 2007, Nature, 445, 892
Saumon, D., Hubbard, W. B., Burrows, A., et al. 1996, ApJ, 460, 993
Segransan, D., Beuzit, J., Delfosse, X., et al. 2000, in SPIE Conf. Ser. 4006, ed. P. Léna, & A. Quirrenbach, 269
Tango, W. J. 1990, AO, 29, 516
Vannier, M., Petrov, R. G., Lopez, B., & Millour, F. 2006, MNRAS, 367, 825
Vasisht, G., & Colavita, M. M. 2004, in SPIE Conf. Ser. 5491, ed. W. A. Traub, 567